Original article

Michele Ferri, Monica Trueba*, Stefano P. Trasatti, Marina Cabrini and Antonietta Lo Conte

Electrochemical investigation of corrosion and repassivation of structural aluminum alloys under permanent load in bending

Abstract: This work reports an electrochemical investigation of corrosion and repassivation in NaCl solutions of structural Al 7075-T6 and Al 2024-T3 as a function of permanent load in bending by means of single-cycle anodic polarization. Experimental variables other than the load level were the extent of corrosion, chloride ion concentration and initial pH of the test solution, in addition to the pre-exposure in the aggressive environment and of the viscosity of the test solution for Al 7075-T6. The susceptibility to local stress during corrosion and repassivation depends on the alloy microstructure and corrosion mechanisms. In the case of Al 2024-T3, the mechanical activation is driven by cathodically controlled dissolution of this alloy at open circuit in concentrated NaCl, being indicative of a chemo-mechanical effect. Conversely, for Al 7075-T6, the effect of applied load is better discerned from the repassivation response. Film rupture/formation sequence and related interfacial (electro)chemical processes determine the stress-enhanced metastable repassivation of this alloy.

Keywords: Al alloys; bending load; electrochemistry; repassivation.

1 Introduction

Repassivation is recognized to start as a stable monolayer of metal oxide is formed at the bottom of a pit (Alkire &

*Corresponding author: Monica Trueba, Università degli Studi di Milano, Dipartimento di Chimica, via Golgi 19, 20133 Milan, Italy, e-mail: monica.trueba@unimi.it
Michele Ferri and Stefano P. Trasatti: Università degli Studi di Milano, Dipartimento di Chimica, via Golgi 19, 20133 Milan, Italy
Marina Cabrini: Università degli Studi di Bergamo, Dipartimento di Ingegneria e Scienze Applicate, viale Marconi 5, 24044 Dalmine (BG), Italy. http://orcid.org/0000-0003-3901-8657
Antonietta Lo Conte: Politecnico di Milano, Dipartimento di Meccanica, via La Masa 1, 20156 Milan, Italy

Ernsberger, 1978; Okada, 1984; Frankel et al., 1996; Sehgal et al., 1998). This is schematically depicted in Figure 1 for a halide aggressive environment. If the rate of formation of oxide nuclei overcomes that of the metal halide, the oxide layer extends and grows in thickness to produce a protective film. The repassivation processes depend on competitive (electro)chemical and metallurgical events in the interfacial reactions (Scully, 1971; Okada, 1984). Studies of Al and Al alloys in chloride-containing solutions have shown that the repassivation response from single-cycle anodic polarization is sensitive to such competitive processes (Yasuda et al., 1990; Pride et al., 1994; Wall & Stoner, 1997; Zhang & Frankel, 2003; Meng & Frankel, 2004; Little et al., 2007; Moore et al., 2008; Jilani et al., 2014; Trueba & Trasatti, 2015; Abreu et al., 2016; Lin et al., 2016). In addition to time effects, material composition and microstructure, test environment, electrochemical condition and mechanical stress determine the occurrence of a potential drop at high currents during the potential scan into the negative direction. The inflection of the reverse curve related to a transition to more occluded local damage has been first proposed by Nisancioglu and Holtan (1978) and experimentally confirmed for Al-Mg and Al-Li-Mg alloys by Moore et al. (2008). The transition supported by the critical pit chemistry have been demonstrated for pure Al (Yasuda et al., 1990; Pride et al., 1994; Frankel et al., 1996; Sehgal et al., 1998) and commercial Al alloys (Nguyen et al., 1982; Moore et al., 2008; Trueba & Trasatti, 2015). Rupture or lifting of the oxide layer due to hydrogen evolution at the metal surface and osmotic pressure effects has been suggested (Pride et al., 1994; Sehgal et al., 1998).
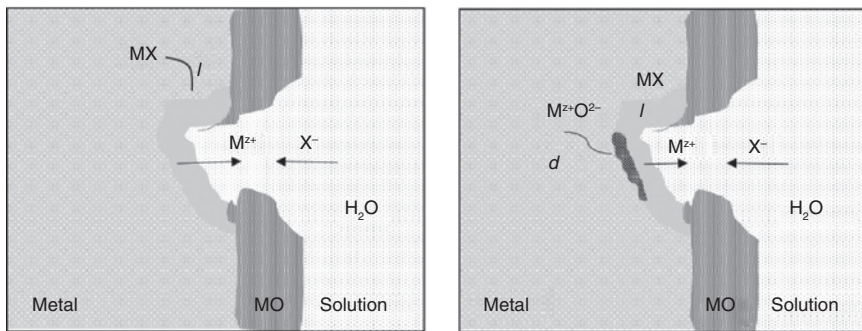
Less straightforward is the interpretation of the repassivation response from single-cycle anodic polarization in the aftermath of microstructural effects (e.g. impurities, precipitate phase, and solute-depleted region) (Wall & Stoner, 1997; Zhang & Frankel, 2003; Meng & Frankel, 2004; Little et al., 2007; Trueba & Trasatti, 2015; Sun et al., 2016). Differently from Al single crystals (Yasuda, et al., 1990) and pure Al (≥99.9%) (Pride et al., 1994; Jilani et al., 2014), no distinguishable transition has been obtained for commercially pure Al 1050 (≥95%), regardless of the

Figure 1: Schematic representation of initial stages of repassivation of an active pit. MX, halide layer at pit bottom; MO, oxide film at the metal surface; M^{z+}, metal ions; X^-, chloride ions; $M^{z+}O^{2-}$, oxide layer at pit bottom; d and l, thicknesses of the oxide and halide layers, respectively.

surface preparation and temper state, as well as different corrosion morphologies (crystallographic pitting and hemispherical etched pits) (Trueba & Trasatti, 2015). Microstructural modifications due to corrosion of Al-Mg alloys, concerning in particular β (Al_3Mg_2) phase precipitation and distribution, influence the transition markedly (Trueba & Trasatti, 2010). This feature as linked to the electrochemistry of a copper depleted region along microstructural boundaries of high strength 2xxx series alloys has been suggested (Wall & Stoner, 1997; Little et al., 2007). Few studies report on the effect of the mechanical state on the response to repassivation (Liu & Frankel, 2006; Jilani et al., 2014; Abreu et al., 2016; Lin et al. 2016). Fine grained Al (99.9%) has shown steeper potential gradients at the transition with accumulated strains by pressing (Jilani et al., 2014), whereas the opposite has been found for Al 2024-T3 subjected to residual elastic compressive stress after uniaxial tensile load (Liu & Frankel, 2006). A correlation between the steepness of the potential drop at the transition onset and residual stress promoted with thermal treatment have been found for Al 2024-T3 and Al 7075-T6 (Trueba & Trasatti, 2015). Abreu et al. (2016) have reported increasing steepness with constant uniaxial tension load up to the yield strength (YS) of Al 2017-T4.

The studies above point out that the sustenance of the aggressive pit-like solution preventing the simultaneous repassivation of all the corroded surfaces is likely determined by equilibrium-limited local cell reactions due to microstructural instability promoted with corrosion. The counterweight of local environment, electrochemical events and possible stress states on the related interfacial (electro)chemical processes is not fully clear. The importance of passive oxide film rupture and regeneration in stress corrosion cracking (SCC) phenomena has been long recognized (Scully, 1971). The coupling between (electro)chemical and mechanical stress raisers producing a sequence of electrochemical processes and

fresh metal surfaces is a critical aspect of the environmentally assisted cracking (EAC) (Sadananda & Vasudevan, 2011). EAC is a primary cause of failure of airframe structural components and other engineering structures with adventitious catastrophic consequences for safety, the environment and economics. Although recognition of EAC mechanisms, improvements in materials selection and inspection methodologies, among other policies, have reduced the severity of such failures, understanding and prediction of the early stages of damage development are hampered by the lack of insight on crack nucleation and growth kinetics, which can be based on different mechanisms for controlling propagation rates. In this respect, high strength and microstructurally complex 2xxx and 7xxx series Al alloys are of major concern.

The present work reports a systematic study of corrosion and repassivation in NaCl solutions of structural Al 7075-T6 and Al 2024-T3 under permanent load in bending by means of single-cycle anodic polarization. The effect of the extent of corrosion, chloride ion concentration and initial pH of the test solution were explored to individuate the testing conditions that point up a dependence of the electrochemical properties on the applied load in bending. The effect of pre-exposure in 0.6 м NaCl (pH 6.5) and of the solution viscosity (by additions of glycerol) were also considered for Al 7075-T6.

2 Materials and methods

2.1 Four-point bent beam stress corrosion test specimens

Aluminum alloys 7075-T6 and 2024-T3 were provided as sheets of 2.0 and 1.5 mm thickness, respectively, by AVIOMETAL S.p.a. (Varese, Italy). The nominal chemical

compositions and mechanical properties are reported in Tables 1 and 2. Four-point bent beam (4PBB) stress-corrosion test specimens were used for application of permanent load in bending with negative deflection (side in tension), as schematically shown in Figure 2. The Al alloy pieces (160 mm×25 mm) were prepared through gig-saw cutting along the rolling direction of the sheet, chain sawing and milling (Grazioli, Brescia, Italy). Before use, the working surfaces were wet ground with abrasive SiC paper up to 1200 grit, thereafter polished with a 3 µm cloth using ethanol (>99.8%, Aldrich) and then cleaned in ethanol using an ultrasonic bath. The samples were mounted in ad hoc designed stainless steel holders (Figure 2), following ASTM 39-99 recommendations (ASTM 1999 Annual Book). Glass or teflon spacers were used to avoid galvanic contact. Permanent load in bending along the longitudinal axis was applied through the loading bolt. The deflection (y) was measured with a dial gauge (±0.01 mm) positioned in the middle of the surface between the inner contact points (loading spans). A strain gauge extensometer (Hottinger-Baldwin-Messtechnik, Darmstadt, Germany) fixed at the upper surface of the 4PBB specimen was used to determine the maximum deformation at the surface (ε_{max}). The average ε_{max}-y plots obtained from three replications for each alloy are reported in Figure 3A. The corresponding maximum bending stress at the surface (σ_{max}) was estimated from the tensile stress-strain curves (Figure 3B). Permanent load in bending up to values of σ_{max} close to YS (100%) were applied.

2.2 Electrochemical experiments

All the experiments were carried out using naturally aerated NaCl solutions that were prepared from the corresponding salt (99.8%, Aldrich) and water of quality MilliQ. An ad hoc designed Pyrex double-walled one-compartment electrochemical cell with a hole at its bottom of 1 cm^2 of area was fixed at the center of 4PBB specimen surface with the help of a bi-adhesive tape. A Pt spiral and a saturated calomel electrode (SCE) were used as counter (or auxiliary) and reference electrodes. SCE was connected to the test solution via a Luggin capillary reference probe. Parallel runs of electrochemical experiments for random testing conditions were performed with the aid of a computer-driven Gamry Interface 1000 multipotentiostat (Gamry Instruments, Warminster, PA, USA). Unless otherwise stated, measurements were performed at room temperature (25±2°C). For reference purposes, 4PBB specimens with no load application (0% YS) were considered also.

Single-cycle anodic polarization curves, herein referred to as pitting scans (PS), were recorded from the open circuit potential at a scan rate of 10 mV/min after 10-min conditioning in the test solution. Potential was scanned in the anodic direction up to a preselected current density limit (i_{rev}) and then reversed until the current became cathodic. For a given load level (ε_{max}), experimental variables such as the extent of corrosion (i_{rev}=1, 2.5 and 5 mA/cm^2), chloride ion concentration ([Cl$^-$]=0.1, 0.3 and 0.6 M), and initial solution pH (3.5±0.2 and 6.5±0.2) were explored.

Table 1: Chemical composition (wt%) of Al alloys[a].

| Al alloy	Si	Fe	Cu	Mn	Mg	Zn	Ti	Cr
7075-T6	0.06	0.13	1.70	0.02	2.60	5.80	0.04	0.20
2024-T3	0.07	0.12	4.40	0.46	1.50	0.08	0.08	0.03

[a]Aviometal Spa (Italy).

Table 2: Mechanical properties of Al alloys[a].

Al alloys	7075-T6	2024-T3
Elastic modulus E (GPa)	74.5	75.7
Yield strength YS, Rp02 (MPa)	510	354
Ultimate tensile strength UTS (MPa)	583	499

[a]From experimental stress-strain curves determined at the Polytechnic Institute of Milan.
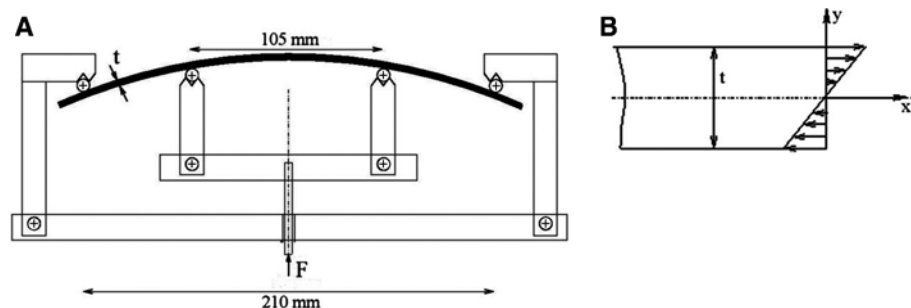
Figure 2: (A) Schematic representation (section view) of four-point bent beam (4PBB) stress corrosion test specimen with negative deflection (side in tension), (B) tensile stress distribution through the width of the beam.
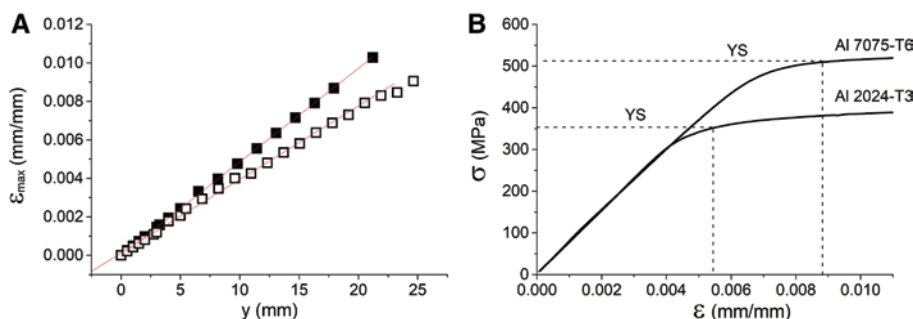
Figure 3: (A) Plots of measured maximum deformation at the surface ε_{max} as a function of the applied negative deflection y: (■) Al 7075-T6, (□) Al 2024-T3. (B) Stress-strain curves for the range of applied deformations where the YS for each alloy is indicated (Table 2).

For Al 7075-T6, the effect of pre-exposure in 0.6 м NaCl, as well as of the test solution viscosity, were investigated also. For the former test variable, 4PBB specimens subjected to different ε_{max} were fully immersed in 0.6 м NaCl (pH 6.5) for different times t_{exp} (from 1 up to 72 h), then rinsed with MilliQ water and dried with hot air before the electrochemical experiment. The viscosity η of 0.6 м NaCl (pH 6.5 and 3.5) was varied with additions of glycerol (propane-1,2,3-triol, >99%, Aldrich) up to 60 wt% (η = 21.5 cP) as measured with a viscosity Ford cup (2 mm) following ASTM D1200 standard practice (ASTM, 2014).

Graphical and quantitative analyses of the experimental data were carried out using OriginPro 2016 program (OriginLab, Northeampton, MA, USA) as detailed elsewhere (Trueba & Trasatti, 2015). Unless otherwise specified, the electrochemical data and the PS reported herein correspond to averaged values from at least two replications.

Selected Al alloy samples were washed with MilliQ water and ethanol (>99.8%, Aldrich), then sectioned along the longitudinal direction and mounted in a cold-working resin. Sectioned surfaces were polished up to 0.05 μm with alumina suspension and chemically etched to reveal grain border, following standard procedures (ASM Handbook, 1985). Corrosion morphology was examined at the Nikon Eclipse MA200 optical microscope (Nikon Instruments, Inc.) and at LEO 1430 scanning electron microscope (SEM) equipped with an energy dispersive spectrometer (Zeiss, Oberkochem, Germany) at a chamber pressure of 8×10^{-6} torr and 20 keV.

3 Results and discussion

3.1 Electrochemical properties from pitting scans in NaCl solutions

Figure 4 shows some typical PS (E-log i plots) recorded for Al 7075-T6 and Al 2024-T3 in naturally aerated NaCl solutions. The PS of the alloys under load were similar and will be discussed in the later sections. For Al 7075-T6 (Figure 4A), two breakdown potentials at E_{pit1} and E_{pit2} are associated to transient dissolution of an active surface layer formed by mechanical polishing and to pitting corrosion across the surface (Zhang & Frankel, 2003; Meng & Frankel, 2004; Hughes et al., 2011; Wang et al., 2013). No passive region is obtained at the beginning of polarization (Figure 4A and B). The as-polished electrode polarizes at the pitting potential E_{pit1} during the 10-min conditioning in the test solution at open circuit due to the presence of dissolved oxygen (Hughes et al., 2011; Wang et al., 2013). The peak-shaped second breakdown became less pronounced as the current density limit of the forward scan i_{rev} was raised, reproducing previous findings (Comotti et al., 2013; Trueba & Trasatti, 2015). The same result was obtained with either the dilution of the test solution or the decrease of the initial pH for a given i_{rev}, though the features of the PS changed little (Figure 4A and B).

Two breakdowns, E_{pit1} and E_{pit2}, are detected for Al 2024-T3 also (Figure 4C), being ascribable to the selective dissolution of Al and Mg in the S (Al-Cu-Mg) phase and to intergranular corrosion (IGC), respectively (Guillaumin & Mankowski, 1998; Zhang & Frankel, 2003; Hughes et al., 2015). The former process promotes copper enrichment of the surface which enhances the kinetics of oxygen reduction ($O_2 + 2H_2O + 4e^- \rightarrow 4OH^-$) (Hughes et al., 2015). The consequent generation of OH^- promotes local pH increase and facilitates localized corrosion. Oscillations of the anodic current below E_{pit1} were eventually recorded and caused poor repeatability of the forward curve (Figure 4D). Nonetheless, replication experiments for data validation indicated that metastable dissolution/passivation events at the beginning of polarization do not significantly influence the electrochemical properties. Differently from Al 7075-T6, the second breakdown is affected by the test conditions (Figure 4C and D). No second breakdown was detected for $[Cl^-] \leq 0.3$ м, regardless of the initial pH of the test solution. The peak in the current recorded for pH 3.5
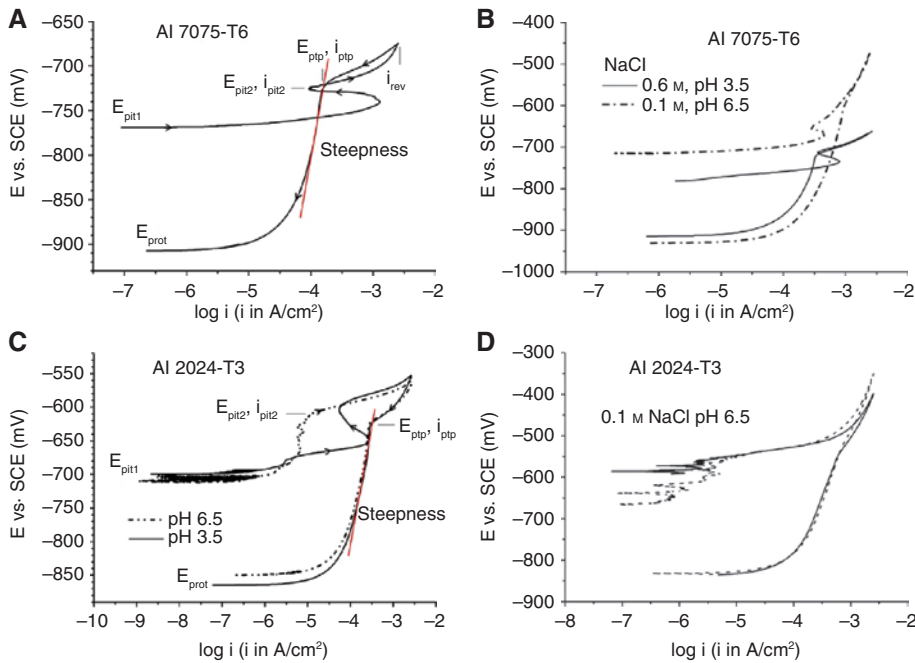
Figure 4: Typical pitting scans of the Al alloys in naturally aerated NaCl solutions for selected test conditions. (A) Characteristic electrochemical properties of Al 7075-T6 (0.6 M NaCl, pH 6.5). E_{pit1} and E_{pit2}, the first and second breakdowns; E_{ptp} and i_{ptp}, the pit transition potential and the associated current density; E_{prot}, the protection potential; i_{rev}, the current density limit of the forward scan; (B) Al 7075-T6, PS for different NaCl concentrations and initial pH; (C) as in (A) for Al 2024-T3 in 0.6 M NaCl, pH 6.5 and 3.5; (D) 2024-T3, two replications of PS; (C, D) 2024-T3, PS for different NaCl concentrations, pH 6.5.

and 0.6 M NaCl (Figure 4C) manifests less favored localization of the attack below the pH range of Al hydroxide stability (pH 4–9).

The repassivation response of both Al 7075-T6 and Al 2024-T3 was featured by an inflection in the reverse curve (Figure 4), indicating a transition to metastable repassivation. This is identified by the pit transition potential E_{ptp} and the associated current density i_{ptp} (Figure 4A and C). From previous studies (Trueba & Trasatti, 2015), E_{ptp} is considered as the thermodynamic driving force of Al dissolution in the acidified pit-like solution in contact with a fresh (filmed) surface. The current density at the inflection is proportional to the rate at which hydrolysis equilibrium is reached at a critical saturation concentration of Al^{3+} (Cicolin et al., 2014) represented by the following general equation to account for the contribution of the OH^- ions at pH higher than 7:

$$2Al^{3+} + H_2O + OH^- \leftrightarrow 2Al(OH)^{2+} + H^+ \qquad (1)$$

Complete repassivation of all the corroded surfaces is associated with the protection potential E_{prot}, that is the potential at which the local activity becomes negligible ($i \leq 10^{-6}$ A/cm²). This consideration is also based on the fact that E_{ptp} becomes indistinguishable from E_{prot} in the absence of an inflection in the reverse curve (Trueba

& Trasatti, 2010; Comotti et al., 2013; Trueba & Trasatti, 2015).

Due to the sluggish metal dissolution through the (hydr)oxide film, high currents driving a potential drop are indicative of mass transport processes favoring local electrodissolution processes and electromigration of Cl^- through the highly conductive salt layer (Figure 1). Thus, the decrease of the potential below E_{ptp} is related to the variation of the electrostatic potential at some distance into the cavities, being driven by the flow of charge across the metal/solution interface proportional to $i \leq i_{ptp}$. Assuming that, under stagnant conditions, the processes above depend only on the potential and their rate depends on the concentrations of Al^{3+} and Cl^- only, the method developed by Engelhardt et al. (1996) for calculating corrosion cavity propagation rates was used to calculate the effective anodic charge transfer coefficient α_{eff} from the steepness of the potential decrease with current below the transition (Figure 4A and C) with the equation (2):

$$\ln \frac{i}{i_{ptp}} = \frac{\alpha_{eff} F}{RT}(E - E_{ptp}) \qquad (2)$$

where E and E_{ptp} are expressed in V (versus SCE), $F = 9.65 \times 10^4$ J/Vmol, $R = 8.31$ J/mol K, and $T = 298$ K.

Considering further that $\alpha_{eff} = \alpha - \lambda$, where α is the anodic charge transfer coefficient and λ is the effective kinetic order of metal dissolution with respect to [Cl⁻] (Engelhardt et al., 1996), α_{eff} estimates the contribution of the electromigration of Cl⁻ for the compensation of the potential drop. From eq. (2), a decrease of α_{eff} corresponds to an increase of the potential gradient and thus to an accelerating action of Cl⁻ ($\alpha \rightarrow \lambda$). The charge transfer coefficient $\alpha_{eff} > 0$ for all the investigated conditions, being consistent with the decrease of the dissolution rate as the potential shifts to E_{prot} (Figure 4).

Henceforth, the results and discussions are focused on those experimental variables that point up a dependence of the electrochemical properties (Figure 4A and C) on the applied ε_{max}. The kinetic properties of repassivation are reported as ratios $i_{ptp,\varepsilon}/i_{ptp,0}$ and $\alpha_{eff,\varepsilon}/\alpha_{eff,0}$, where the subscripts ε and 0 identify the average values obtained with ($\varepsilon_{max} \neq 0$) and without ($\varepsilon_{max} = 0$) load application.

3.2 Extent of corrosion

The combined effect of the extent of corrosion and applied deformation was investigated in 0.6 M NaCl with initial pH of 6.5 and 3.5, using different current density limits of the forward scan ($i_{rev} = 1$, 2.5 and 5 mA/cm²) (Figure 4A and C). Figure 5 reports the potentials as a function of ε_{max}. Mean $\bar{E}$ corresponds to average potential taken for overall the data for a given ε_{max} in those cases where either or both i_{rev} and pH cause negligible variations. It is appreciated that the applied deformation does not influence the potentials for Al 7075-T6 (Figure 5A). Only the characteristic potentials of repassivation E_{ptp} and E_{prot} for pH 6.5 change with i_{rev}. The $E_{ptp} - \varepsilon_{max}$ and $E_{prot} - \varepsilon_{max}$ plots shift with the extent of corrosion to higher and smaller potential values, respectively. For a given bulk [Cl⁻], the ennoblement of E_{ptp} indicates

changes in local surface and solution compositions due to microstructural evolution with corrosion (Comotti et al., 2013; Trueba & Trasatti, 2015), whereas the decrease of E_{prot} indicates that repassivation of all the corroded surfaces becomes less favored. These opposite trends suggest increasing copper content in grain boundary precipitates (GBP) that inhibits the crack tip activity (Knight et al., 2010) but promotes flaws on the oxide layer at the metal surface (Gibbs free energies of copper oxide formation per equivalent ($\Delta G°/n$) are higher than for alumina) (Hughes et al., 2011).

In the case of Al 2024-T3 (Figure 5B), only $\bar{E}_{pit1}$ (mean values taken for overall the data for different i_{rev}) for pH 6.5 changes markedly. This potential decreases with ε_{max} up to about 0.005 mm/mm and then shifts to less negative values as ε_{max} is raised further. Taking into account that $E_{pit1} \approx E_{corr}$ (Figure 4C) the above mentioned trend is determined by corrosion processes that were readily promoted at open circuit prior to the anodic polarization. The disennobling of E_{pit1} up to ε_{max} (≈ 0.005 mm/mm) indicates a decrease of the polarization resistance as a consequence of mechanical activation of the anodic processes. However, the increase of $\bar{E}_{pit1}$ (and thus of the polarization resistance) as ε_{max} approaches values close to the YS is difficult to explain considering a mechanical action only. Similar indication is given by the no dependence of $\bar{E}_{pit1}$ on ε_{max} for pH 3.5 (Figure 5B), as well as by the no effect of ε_{max} on E_{pit1} for Al 7075-T6 (Figure 5A). These differences must be linked to the nature of the alloys. Local (electro) chemical interactions between the stressed metal and the environment depend on the microstructure and corrosion mechanisms.

Although mechanical deformation exerts a slight effect on the cathodic processes, the extent of disennobling of the steady state potential and of corrosion current change depend on the effect of mechanical stress on the kinetics
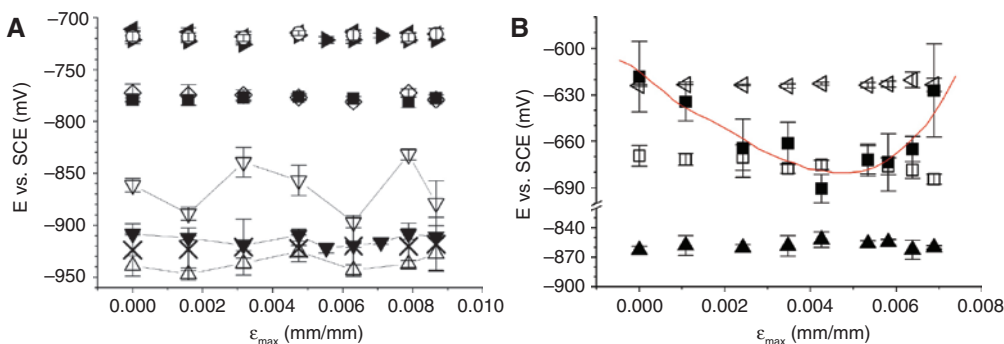

Figure 5: Plots of electrochemical potentials as a function of ε_{max} for (A) Al 7075-T6 and (B) Al 2024-T3, from PS in 0.6 M NaCl for different pH (6.5 and 3.5) and i_{rev} (1, 2.5 and 5 mA/cm²). (A) (■) $\bar{E}_{pit1}$ (i_{rev}, pH) (◇, ▶, ○) E_{ptp}, pH 6.5, $i_{rev} = 1$, 2.5 and 5 mA/cm², respectively; (▽, ▼, △) E_{prot}, pH 6.5, $i_{rev} = 1$, 2.5 and 5 mA/cm², respectively; (B) (■) E_{pit1} (i_{rev}), pH 6.5; (▢) E_{pit1} (i_{rev}), pH 3.5; (◁) $\bar{E}_{ptp}$ (i_{rev}, pH) (▲) $\bar{E}_{prot}$ (i_{rev}, pH).

of anodic and cathodic reactions (Gutman, 1994). S-phase particles are recognized to undergo Al and Mg loss under open circuit conditions, leaving behind Cu sponge-like deposits that facilitate oxygen reduction (Hughes et al., 2015). This favors the development of local corrosion elements of galvanic couple type at the surface. Pitting corrosion is cathodically driven by oxygen reduction on small Cu cathodes that promote localization of corrosion processes and contribute to flaw development on the growing Al (hydr)oxide corrosion film. The mechanical activation manifested by the disennobling of E_{pit1} with ε_{max} within the elastic region of deformation discloses a chemomechanical effect (Gutman, 1994), similar to a Rehbinder effect (Rehbinder & Shchukin, 1972; Revie, 1983). The enhanced dissolution in the vicinity of dislocations generates vacancies able to accelerate the dislocation mobility and thus the plastic flow. This phenomenon has been designated as anodic attenuation of strain hardening by Jones (1996). The weakening of the chemomechanical effect as load levels approach YS could be ascribed to a barrier action of corrosion products film hindering the exit of dislocations from the surface and thus inhibiting the creation of fresh surfaces (Revie, 1983). The no manifestation of chemomechanical effect for pH 3.5 (Figure 5B) indicates that localization of anodic processes and the development of micro-electrochemical heterogeneity determine the stress-environment interactions. The relative contribution of the kinetics of anodic and cathodic reactions is supported further by no variation of E_{pit1} in the case of Al 7075-T6 (Figure 5A), which corrodes under minimal cathodic control at open circuit. Al_7Cu_2Fe particles behave as net cathodes but with small cathodic current densities; Mg_2Si inclusions have large anodic current densities but eventually give silicon-rich deposits; and the microgalvanic coupling between η-$MgZn_2$ phase precipitates and the adjacent matrix provides the driving force for grain boundary activity. It is to be noticed that E_{ptp} is ε_{max}-independent for both alloys (Figure 5). The same result was obtained for E_{pit2}. Both potentials correspond to predominant anodic dissolution processes driven by external polarization.

With regards to the repassivation response, the variability of the plots $i_{ptp,\varepsilon}/i_{ptp,0}-\varepsilon_{max}$ and $\alpha_{eff,\varepsilon}/\alpha_{eff,0}-\varepsilon_{max}$ is more significant for both alloys in near-neutral NaCl (Figure 6). Considering first the effect of i_{rev}, the $i_{ptp,\varepsilon}/i_{ptp,0}-\varepsilon_{max}$ plots shift to smaller values with the extent of corrosion in the case of Al 7075-T6 (Figure 6A, filled squares, from top to bottom). The corresponding $\alpha_{eff,\varepsilon}/\alpha_{eff,0}-\varepsilon_{max}$ plots (Figure 6B, filled squares, from top to bottom) show $\alpha_{eff,\varepsilon}/\alpha_{eff,0}>1$ for $i_{rev}=5$ mA/cm² only. That is, the potential gradient at the transition onset (2) decreases with the

extent of corrosion ($\alpha_{eff,\varepsilon}>\alpha_{eff,0}$) regardless of the applied ε_{max}. Considering further that $i_{ptp,\varepsilon}\approx i_{ptp,0}$ for $i_{rev}=5$ mA/cm², metastable repassivation and the accompanying electromigration of Cl⁻ tend to be less favored. This correlates with the shift of E_{ptp} to less negative values (Figure 5A), ascribable to the increase of Cu content in GBP. Correspondingly, the negative shift of E_{prot} with i_{rev} (Figure 5A) is associated to diffusion-limited repassivation. The results for Al 2024-T3 are different (Figure 6A and B, empty circles). The trends of the plots $i_{ptp,\varepsilon}/i_{ptp,0}-\varepsilon_{max}$ and $\alpha_{eff,\varepsilon}/\alpha_{eff,0}-\varepsilon_{max}$ indicate an increase of $i_{ptp,\varepsilon}$ and a decrease of $\alpha_{eff,\varepsilon}$ with respect to $i_{ptp,0}$ and $\alpha_{eff,0}$ (no load application) as i_{rev} is raised. The contrasting effect of i_{rev} on the repassivation kinetic parameters of Al 7075-T6 and Al 2024-T3 suggests that i_{ptp} is not solely determined by the amount of corroded surfaces under load in bending but is responsive to the propensity of anodic processes localization. This consideration is supported by the complex variation of $i_{ptp,\varepsilon}/i_{ptp,0}$ and $\alpha_{eff,\varepsilon}/\alpha_{eff,0}$ with ε_{max} (Figure 6). Although such complex trends could result from changes in local stresses along the length and across the width of the specimen, both alloys show a linear decrease of $\alpha_{eff,\varepsilon}/\alpha_{eff,0}$ with ε_{max} with similar gradient lines for $i_{rev}=2.5$ mA/cm², regardless of the well-different $i_{ptp,\varepsilon}/i_{ptp,0}-\varepsilon_{max}$. That is, $i_{ptp,\varepsilon}$ increases with respect to $i_{ptp,0}$ as ε_{max} is raised up to about 90% YS in the case of Al 7075-T6, whereas the opposite is likely for Al 2024-T3 ($i_{ptp,\varepsilon}/i_{ptp,0}<1$). Taking into account that local dissolution processes at microscale tend to decelerate with the reverse potential scan, the decrease of $\alpha_{eff,\varepsilon}/\alpha_{eff,0}$ (i.e. the increase of the steepness, Figure 4A and C) with ε_{max} manifests a prevailing mechanochemical effect (Gutman, 1994). That is, local stress-environment interactions enhance metastable electrodissolution processes and contribute to localization of anodic processes during repassivation. The fact that the current density limit of 2.5 mA/cm² allows for a higher sensitivity of α_{eff} to local stresses regardless of the alloy nature points to a critical electrochemical condition for stress-assisted dissolution processes. Recall of previous studies of these alloys under similar experimental conditions but with no load application indicated a change in the morphology of corrosion at $i_{rev}=2.5$ mA/cm² (Comotti et al., 2013). That is, from a prevalent intergranular (IG) attack to transgranular dissolution in the case of Al 7075-T6 and to microstructural pitting in the case of Al 2024-T3 (no second breakdown was detected for this alloy). It is likely that stress-enhanced metastable repassivation is intensified at the borderline of such transitions.

Corrosion morphology analysis indicated some correlation between the prevalence of narrow and extended crack paths and the variation of $i_{ptp,\varepsilon}/i_{ptp,0}$ and $\alpha_{eff,\varepsilon}/\alpha_{eff,0}$ for Al 7075-T6 (Figure 6). Micro cracks and voids due to crack
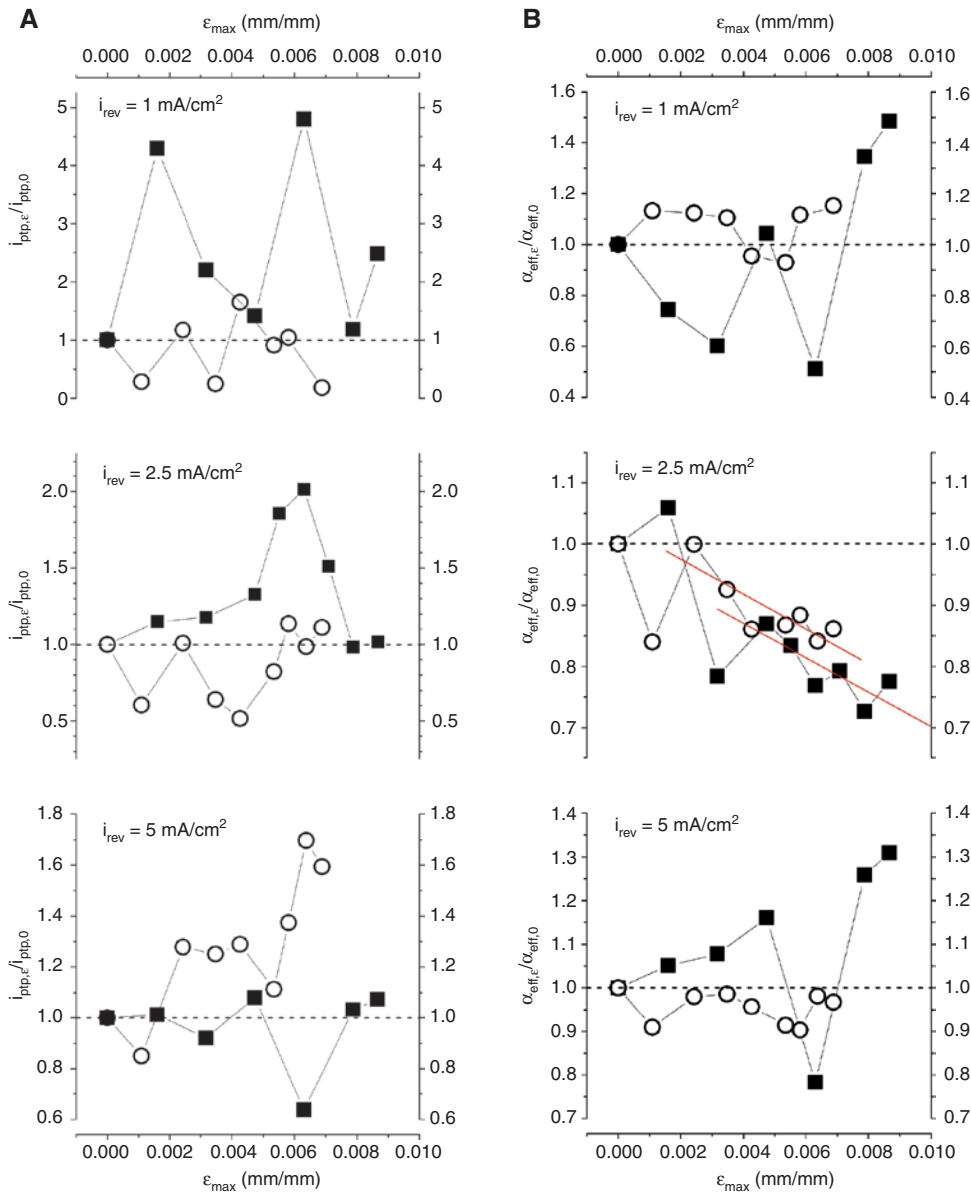
Figure 6: Plots of (A) $i_{ptp,\varepsilon}/i_{ptp,0}$ and (B) $\alpha_{eff,\varepsilon}/\alpha_{eff,0}$ as a function of ε_{max} for (■) Al 7075-T6 and (○) Al 2024-T3 for different i_{rev}. Data obtained from PS recorded in 0.6 M NaCl (pH 6.5), $\nu = 10$ mV/min.

coalescence were promoted for $i_{rev} \leq 2.5$ mA/cm² and YS $\geq$ 90% (Figure 7A). Hairline cracks oriented 45° with respect to the surface were detected for $i_{rev} = 2.5$ mA/cm² and 90% YS only (Figure 7B), suggesting this load condition favoring shear stresses localization under confining pressures originated at corrosion-activated local surface defects (Tyzak, 1971; West, 1980; Gutman, 1994; Callister, 2006). Examination of corroded specimens under similar conditions but pH 3.5 indicated crack propagation parallel to the direction of the applied load (Figure 7C).

The occurrence of hairline cracking below the macroscopic YS has been associated to an increase of the

hydrostatic pressure in local regions like dislocation intersections, while the remaining solid obeys the elasticity laws (Ziman, 1964; Gutman, 1994). Within limited volumes of such imperfections, these sites take up the entire load and transmit it to adjacent regions of the solid matrix. From studies of Al alloys in NaCl solutions containing either H_2O_2 as passivator or Cl^- as inhibitor of uniform anodic dissolution (Gutman, 1994), the contribution of dislocations to the mechanochemical effect at shearing stress below YS is enhanced if the anodic dissolution starts from the same places with and without load application. A high density of dislocations along the
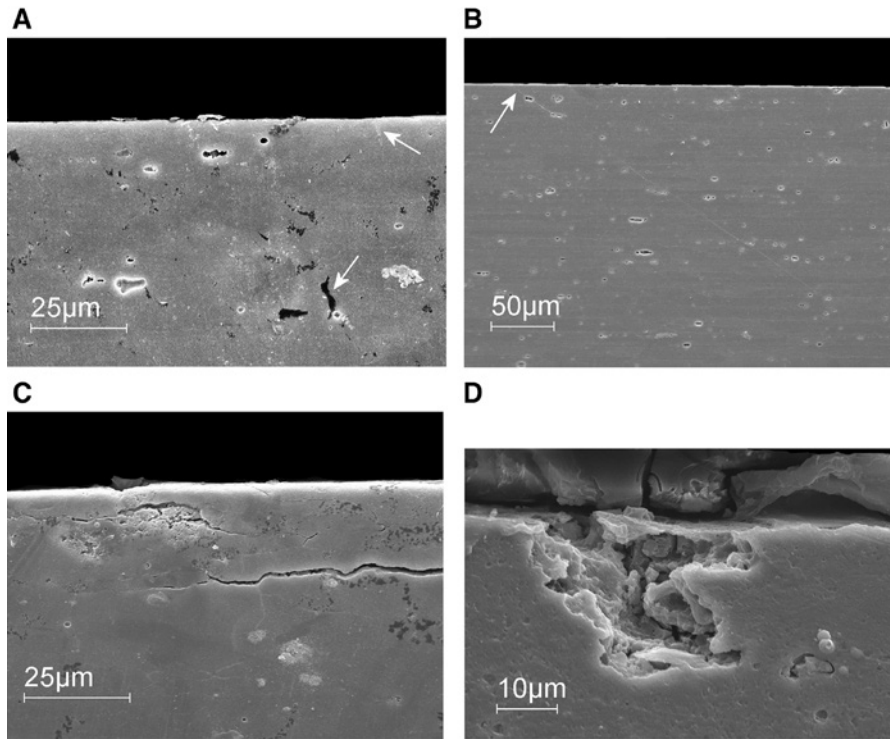
Figure 7: Section SEM images of (A–C) Al 7075-T6 and (D) Al 2024-T3, after PS in 0.6 M NaCl for different pH, i_{rev} and applied load: (A) 6.5; 1 mA/cm^2, 100% YS; (B) 6.5; 2.5 mA/m^2, 90% YS; (C) 3.5; 2.5 mA/cm^2, 100% YS; and (D) 6.5; 2.5 mA/m^2; 100% YS.

interface between the surface layer formed during surface preparation by mechanical polishing and the bulk matrix is typical of 7xxx series Al alloys (Wang et al., 2013). This characteristic could explain the development of hairline cracking below the macroscopic YS. The enhanced dissolution of the surface layer at pH 3.5 likely determines the prevalent action of longitudinal stresses assisted by the electrochemical activity of the η-phase (MgZn$_2$) and local production of hydrogen along grain boundaries (Lynch, 2012; Knight et al., 2015). It is to be noticed that $\alpha_{eff,\varepsilon}/\alpha_{eff,0}$ values were similar for both pH but $i_{ptp,\varepsilon}/i_{ptp,0} \approx 1$ for all ε_{max} in the case of acidified test solution. Film rupture and formation sequence as a result of the joined action of (electro) chemical processes and mechanical stress seems to be a critical factor. No distinct morphology was observed for Al 2024-T3, which prevalently suffered pitting corrosion. Narrow cracks within large pits resulted evident for $i_{rev} = 2.5$ mA/cm^2 only (Figure 7D), in correspondence with the decrease of $\alpha_{eff,\varepsilon}/\alpha_{eff,0}$ with ε_{max} (Figure 6).

Summing up the above results, the electrochemical potentials are responsive to the applied deformation if mechanical stress affects anode and cathode kinetics such as to induce microstructural instability as in the case of Al 2024-T3. The kinetic properties of repassivation are responsive to the applied deformation for both alloys, provided that the extent of corrosion is moderate

(2.5 mA/cm^2). Al 7075-T6 is more prone to localization of anodic processes in combination with local stress during repassivation.

3.3 Chloride ion concentration

The experiments carried out using less concentrated NaCl solutions ([Cl$^-$] = 0.1 and 0.3 M, pH 6.5) and $i_{rev} = 2.5$ mA/ cm^2 indicated no significant effect of ε_{max} on the potentials for both alloys. The linear relationships between the mean E and log [Cl$^-$] closely reproduce previous results (Trueba & Trasatti, 2015), as illustrated for Al 7075-T6 in Figure 8A. The different slopes of E_{pit1}-log [Cl$^-$] plots for [Cl$^-$] ≥ 0.3 M in the case of Al 2024-T3 (Figure 8B) are due to the significant variation of E_{pit1} with ε_{max} in 0.6 M NaCl (pH 6.5) (Figure 5B). The fact that dissolution-enhanced plastic flow is revealed for the more aggressive test solution points out that the joint action of mechanical stress and environment on reducing the surface energy are important for this alloy. Present findings emphasize further the competition between the destabilization of the oxide film adjacent to Cu-rich particles, the film formation and the cathodic reactions, as well as corrosion-related crack initiation, which is closely related to interacting pits through IG attack under loading (Hughes et al., 2015).
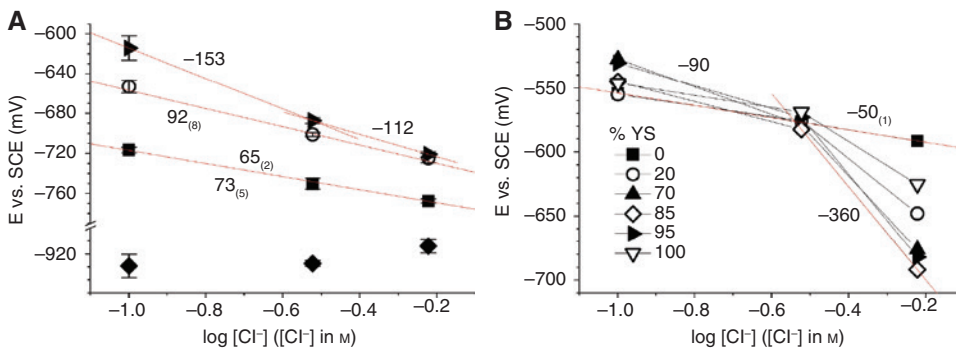
Figure 8: (A) Plots of the characteristic potentials as a function of log [Cl⁻] (pH 6.5) for Al 7075-T6: (■) $\bar{E}_{pit1}$; (○) $\bar{E}_{pit2}$ (▶) $\bar{E}_{ptp}$; (◆) $\bar{E}_{prot}$; error bars represent standard deviation of the mean values taken from all the data at different ε_{max}. (B) Plots of E_{pit1} as a function of log [Cl⁻] (pH 6.5) for Al 2024-T3 and different applied loads (indicated in the label). Data derived from experimental PS curves using $i_{rev} = 2.5$ mA/cm².

Figure 9 reports the plots of $i_{ptp,\varepsilon}/i_{ptp,0} - \varepsilon_{max}$ and $\alpha_{eff,\varepsilon}/\alpha_{eff,0} - \varepsilon_{max}$ for Al 7075-T6. While $i_{ptp,\varepsilon}/i_{ptp,0} < 1$ for all ε_{max} in the case of 0.1 M NaCl only (Figure 9A), $\alpha_{eff,\varepsilon}/\alpha_{eff,0} < 1$ for all [Cl⁻] (Figure 9B). In addition, the $\alpha_{eff,\varepsilon}/\alpha_{eff,0} - \varepsilon_{max}$ plots are closely overlapped, indicating a negligible effect of [Cl⁻]. Recall of previous studies with no applied deformation (Trueba & Trasatti, 2015) indicated that both i_{ptp} and the steepness increase with dilution of the test solution due to higher concentration gradients between the occluded cavities and outer bulk solutions. In this study, the increase of $i_{ptp,\varepsilon}$ in relation to $i_{ptp,0}$ is more significant as the test solution is made more aggressive. Accordingly, metastable repassivation under load is not driven by concentration gradients only but is enhanced due to local stress-environment interactions. Transgranular attack was the prevalent corrosion morphology revealed in the absence of applied load (Figure 10A). Conversely, IG corrosion and discontinuous micro-crack nucleation at the base of IG-corroded paths prevailed with load application and with increasing deformation for 0.1 M NaCl, regardless of the pH (Figure 10B and C). As for 0.6 M NaCl (pH 6.5)

and 90% YS (Figure 7B), hairline cracking was detected for the diluted test solution at pH 3.5 (Figure 10D). For this test condition, $\alpha_{eff,\varepsilon}/\alpha_{eff,0}$ values and the variation of $i_{ptp,\varepsilon}/i_{ptp,0}$ with ε_{max} resembled closely those for 0.6 M NaCl (pH 6.5) (Figure 9A and B). Accordingly, an increase of $i_{ptp,\varepsilon}/i_{ptp,0}$ for $\alpha_{eff,\varepsilon}/\alpha_{eff,0} < 1$ manifests mechanochemical interactions favoring crack nucleation and propagation. The load of 90% YS corresponds to the mechanical condition that provides sufficient non-uniform stress distribution due the coexistence of elastic and plastic regions at microscale (microyielding). From the analysis of the reaction orders with respect to [Cl⁻], estimated from the slopes of log i_{ptp}-log [Cl⁻] plots as detailed elsewhere (Cicolin et al., 2014; Trueba & Trasatti, 2015), fractional reaction orders of about 0.5 (on average) are obtained for ε_{max} between 0.005 and 0.008 mm/mm for all [Cl⁻] and pH (Figure 11). This is consistent with local generation of hydrogen due to anodic dissolution of η phase. The fact that IG attack in addition to small discontinuous microcracks through the lattice were less evident for pH 6.5 (Figures 7A, B and 10B–D) points out that the preferential paths for hydrogen
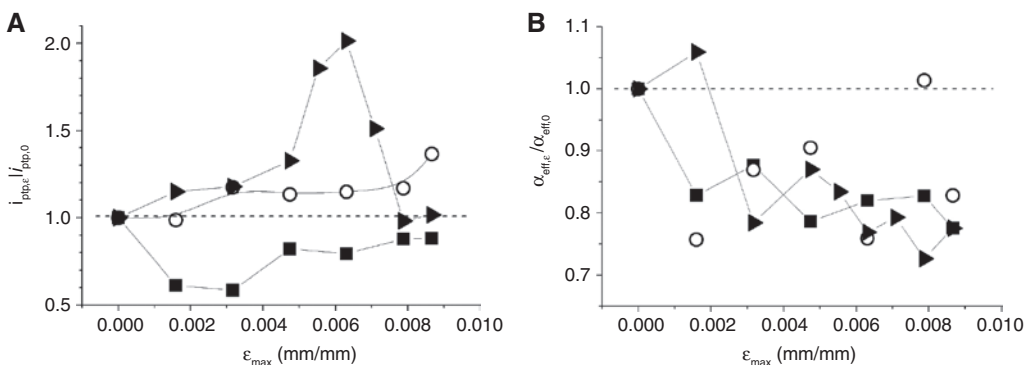
Figure 9: Plots of (A) $i_{ptp,\varepsilon}/i_{ptp,0}$ and (B) $\alpha_{eff,\varepsilon}/\alpha_{eff,0}$ as a function of ε_{max} for Al 7075-T6 and different [Cl⁻] (M): (■) 0.1; (○) 0.3; (▶) 0.6. Data obtained from PS recorded in 0.6 M NaCl (pH 6.5), $\nu = 10$ mV/min.
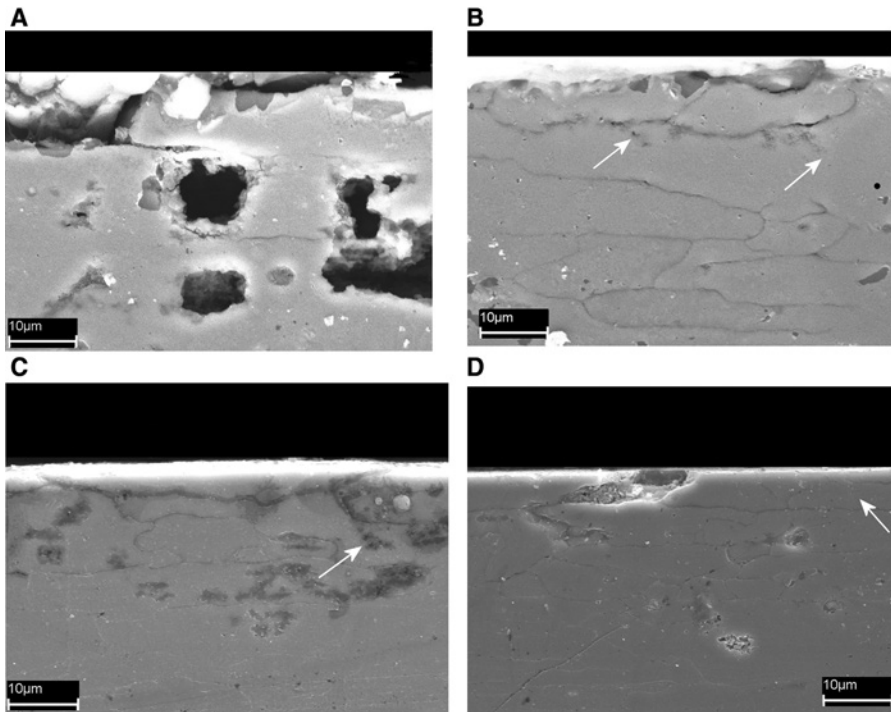
Figure 10: Section SEM images of Al 7075-T6 after PS (i_{rev} = 2.5 mA/cm^2) in 0.1 M NaCl at different pH: (A) 0% YS, pH 6.5; (B) 100% YS, pH 6.5; (C, D) 90% YS, pH 3.5.
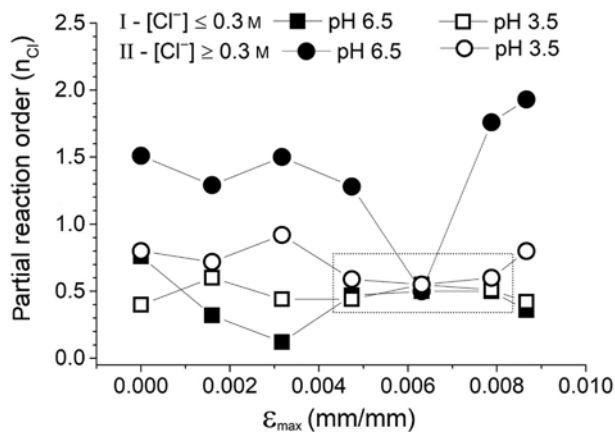
Figure 11: Plots of the partial reactions orders with respect to [Cl$^-$] (n_{Cl}) as a function of ε_{max} for Al 7075-T6. The values of n_{Cl} correspond to the absolute slopes of log i_{ptp}-log [Cl$^-$] plots for (I) [Cl$^-$] ≤ 0.3 M and (II) [Cl$^-$] ≥ 0.3 M, pH 6.5 and pH 3.5.

diffusion are determined by the stability of the surface layer formed by mechanical polishing.

Both $i_{ptp,\varepsilon}/i_{ptp,0}$ and $\alpha_{eff,\varepsilon}/\alpha_{eff,0}$ significantly fluctuate with ε_{max} for Al 2024-T3 (Figure 12A and B). No evident trend for the effect of [Cl$^-$] emerges. The $i_{ptp,\varepsilon}/i_{ptp,0}$ and $\alpha_{eff,\varepsilon}/\alpha_{eff,0}$ values are (on average) smaller than those obtained for Al 7075-T6 (Figure 9A and B). In addition, n_{Cl} values were between 0.2 and 0.4 for [Cl$^-$] ≤ 0.3 M and between 0.8 and

2.0 for [Cl$^-$] ≥ 0.3 M. Although fractional orders (≤0.4) correlate with microcracks at grain boundaries (Figure 13), large cavities at some distance from the surface that grow in the direction of the applied deformation were the dominant corrosion morphology, regardless of ε_{max}.

3.4 Pre-exposure in aggressive environment and viscosity

Pre-exposure embrittlement is of crucial importance in the SCC behavior of 7xxx series Al alloys (Holroyd & Scamans, 2011). In turn, glycerol has been proposed as an alternative non-corrosive medium to the laboratory air for evaluating SCC of high strength aluminum alloys (Bobby Kannan et al., 2004). Correspondingly, the effect of pre-exposure in 0.6 M NaCl (pH 6.5) and of the solution viscosity (by additions of glycerol) on the electrochemical response to corrosion and repassivation of Al 7075-T6 were considered. The diffusion coefficient of glycerol in water mixtures at 20°C (D≈10^{-7} cm^2/s) should not change with glycerol concentration up to 70 wt% because of the disfavored hydration of glycerol molecules (Nishijima and Oster, 1960).

The pre-exposure time (t_{exp}) causes a shift of E_{pit1} to less negative values, regardless of ε_{max} (Figure 14A). The data obtained under similar test conditions with no
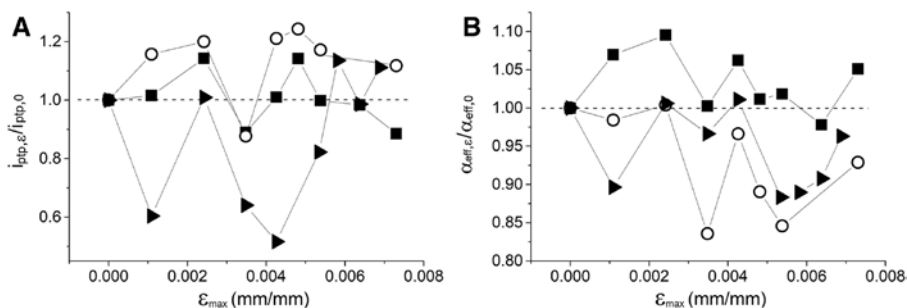
Figure 12: Plots of (A) $i_{ptp,\varepsilon}/i_{ptp,0}$ and (B) $\alpha_{eff,\varepsilon}/\alpha_{eff,0}$ as a function of ε_{max} for Al 2024-T3 and different [Cl⁻] (M): (■) 0.1; (○) 0.3; (▶) 0.6. Data obtained from PS recorded in 0.6 M NaCl (pH 6.5), $\nu = 10$ mV/min.
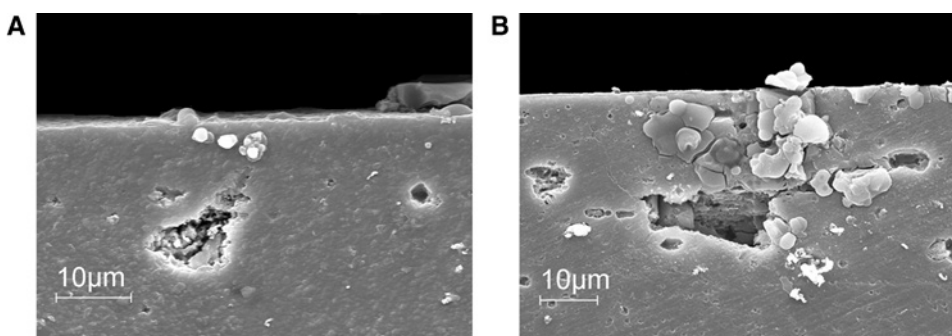
**Figure 13:** Section SEM images of Al 2024-T3 after PS in 0.1 M NaCl (pH 6.5), $i_{rev} = 2.5$ mA/cm², for different applied bending deformation (side in tension): (A) 50% YS; (B) 100% YS.
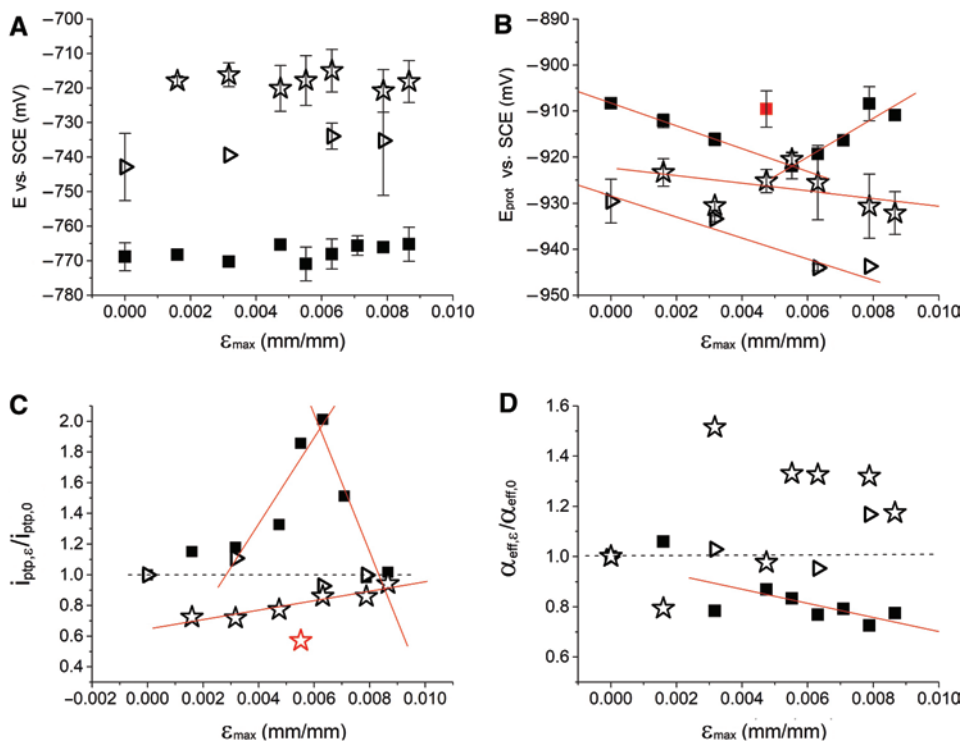
Figure 14: (A, B) Plots of E_{pit1} and E_{prot} as a function of ε_{max} for different pre-exposure times t_{exp} in 0.6 M NaCl (pH 6.5): (■) 0 h (10 min conditioning in the test solution prior to anodic polarization), (▷) 15 h, (☆) 72 h, error bars represent the standard deviation. (C, D) Plots of the ratios $i_{ptp,\varepsilon}/i_{ptp,0}$ and $\alpha_{eff,\varepsilon}/\alpha_{eff,0}$ as a function of ε_{max} for the t_{exp} in (A, B). Symbols in red color are masked points for linear fitting. Data obtained from PS recorded 0.6 M NaCl (pH 6.5), $\nu = 10$ mV/min, $i_{rev} = 2.5$ mA/cm².
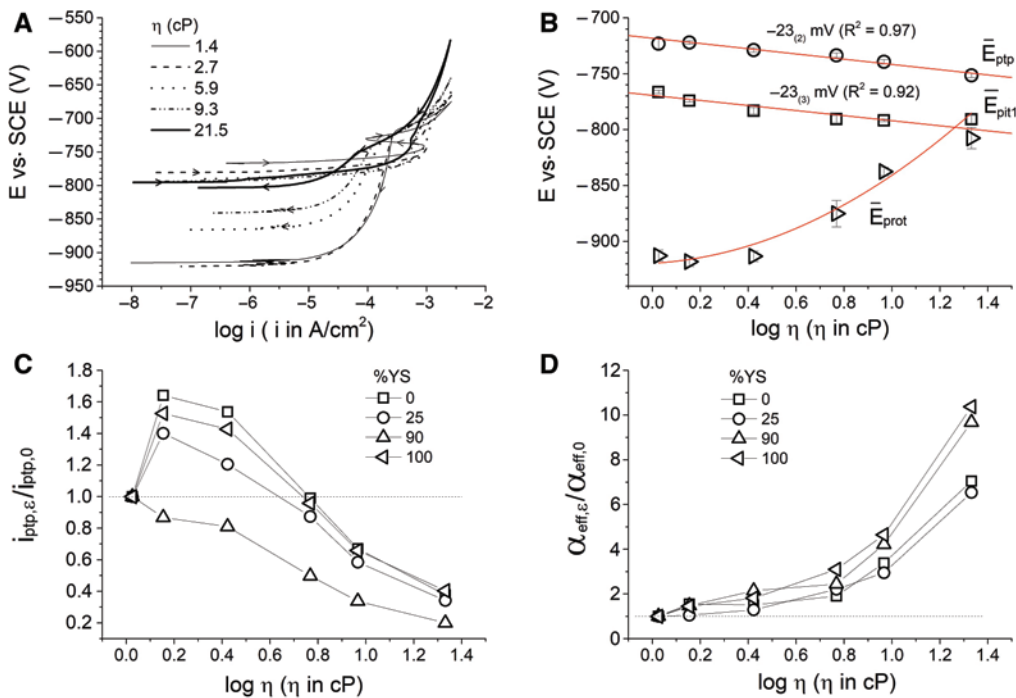
Figure 15: (A) Pitting scans of Al 7075-T6 in 0.6 M NaCl containing different amount of glycerol. The viscosiy of the test solution is reported in the label; (B) Plots of mean electrochemical potentials $\bar{E}_{pit1}$, $\bar{E}_{ptp}$ and $\bar{E}_{prot}$ as a function of log η; (C, D) plots of log ($i_{ptp,\varepsilon}/i_{ptp,0}$) and log ($\alpha_{eff,\varepsilon}/\alpha_{eff,0}$) as a function of log η for different applied loads in bending: 25, 90 and 100% YS ($\varepsilon_{max} \approx 0.002$, 0.006 and 0.009 mm/mm, respectively). The unload condition is indicated as 0% YS. Data obtained from PS ($\nu = 10$ mV/min, $i_{rev} = 2.5$ mA/cm^2) of Al 7075-T6 in 0.6 M NaCl solutions (pH 6.5 and 3.5) containing different amounts of glycerol (up to 60 wt%).

pre-exposure (Figures 5A and 6, $i_{rev} = 2.5$ mA/cm^2) are included for comparison. No second breakdown was detected for all $t_{exp} > 0$, whereas E_{ptp} changed little with both t_{exp} and ε_{max} (−720 ± 10 mV versus SCE). The variation of E_{prot} with ε_{max} is not as significant as that with t_{exp} (Figure 14B). The corresponding plots shift to more negative values up to $t_{exp} \approx 15$ h, while the effect of ε_{max} becomes less important with prolonged pre-exposure (72 h). In addition, comparatively, $i_{ptp,\varepsilon}/i_{ptp,0} \rightarrow 1$ and $\alpha_{eff,\varepsilon}/\alpha_{eff,0} \rightarrow 1$ with t_{exp} (Figure 14C and D). These electrochemical results indicate that the effect of ε_{max} on either the electrochemical potentials or repassivation kinetic properties is negligible. Pre-exposure in 0.6 M NaCl disfavors localized attack during anodic polarization but aids repassivation due to the recovery ability of the Al (hydr)oxide film, in which elasticity could mask possible mechanochemical interactions under load.

The effect of the test solution viscosity (η) was considered for pH 6.5 and 3.5 with no pre-exposure ($t_{exp} = 0$ h). As above, no significant effect of ε_{max} on the electrochemical potentials is obtained. Figure 15A shows the plots of the mean values ($\bar{E}$), taken for overall the data for a given ε_{max} and pH, as a function of log η. Linear relationships with negative (and equal) slopes for $\bar{E}_{pit}$ and $\bar{E}_{ptp}$ provide confirmation that these potentials are closely related. A

quadratic equation fitted best the increase of $\bar{E}_{prot}$ with log η ($R^2 > 0.9$) that manifests a significant decrease of the size of the hysteresis loop between the forward and reverse curves (Figure 4A). The $i_{ptp,\varepsilon}/i_{ptp,0}$ and $\alpha_{eff,\varepsilon}/\alpha_{eff,0}$ ratios changed with log η markedly also, but differences due to the mechanical state are better discerned. In particular, the log-log plots of $i_{ptp,\varepsilon}/i_{ptp,0}$ versus η show a linear decrease of $i_{ptp,\varepsilon}/i_{ptp,0}$ with closely equal slopes for all the load levels but are shifted to $i_{ptp,\varepsilon}/i_{ptp,0} < 1$ for 90% YS only (Figure 15C). Nonetheless, $\alpha_{eff,\varepsilon}/\alpha_{eff,0} > 1$ and the corresponding log-log plots shift parallel to higher values as both viscosity and ε_{max} increase (Figure 15D). This indicates that the compensation of the potential drop by electromigration of Cl$^-$ decreases and becomes comparable for high loads and higher η. Correspondingly, changes in the local chemistry due to adsorption of OH groups of the polyol on the surface limit localized attack and favor repassivation under load.

4 Conclusions

The corrosion and repassivation in NaCl solutions were studied for Al 7075-T6 and Al 2024-T3 as a function of the

applied load in bending up to the YS by means of single-cycle anodic polarization. Among the electrochemical potentials, only E_{pit1} for Al 2024-T3 changes with the applied load in bending but below the macroscopic YS. The disennobling of this potential associated to mechanical activation, namely, the acceleration of dislocation mobility and thus of plastic flow, is driven by the cathodically controlled dissolution at open circuit. In addition to the microstructural instability promoted with corrosion, the joined action of mechanical stress and aggressive environment on reducing the surface energy of the alloy is necessary for a manifestation of the chemomechanical effect.

The kinetic properties of repassivation vary more significantly with the applied load for both alloys. Metastable repassivation is not driven by concentration gradients only under permanent load in bending but is stress-enhanced due to further localization of anodic processes with repassivation. Mechanochemical effects associated to the activation of dislocations at the interface between the surface layer and the bulk matrix of Al 7075-T6 are better discerned from the repassivation response. The film rupture and formation sequence is mostly affected by the joined action of (electro)chemical interfacial processes and mechanical stress.

References

Abreu CM, Cabeza M, Feijoo I. Study of surface corrosion on AA 2017-T4 aluminum alloy by using electrochemical parameters. Surf Interface Anal 2016; 48: 676–679.

Alkire R, Ernsberger D. Occurrence of salt films during repassivation of newly generated metal surfaces. J Electrochem Soc 1978; 125: 1382–1388.

Annual Book of ASTM Standards. Standard practice for preparation and use of bent-beam stress-corrosion test specimens. Philadelphia: ASTM International, 1999.

ASM Handbook. Vol. 9: Metallography and microstructure. Materials Park, Ohio: ASM International, 1985.

ASTM D1200-10 (2014). Standard Test Method for Viscosity by Ford Viscosity Cup. West Conshohocken, PA: ASTM International, 2014.

Bobby Kannan M, Raja VS, Mukhopadhyay AK. Determination of true stress corrosion cracking susceptibility index of a high strength Al alloy using glycerin as the non-corrosive atmosphere. Scripta Mater 2004; 51: 1075–1079.

Callister WD Jr. Materials science and engineering. An introduction. New York: John Wiley & Sons, Inc., 2006.

Cicolin D, Trueba M, Trasatti SP. Effect of chloride concentration, pH and dissolved oxygen, on the repassivation of 6082-T6 Al alloy. Electrochim Acta 2014; 124: 27–35.

Comotti I, Trueba M, Trasatti SP. The pit transition potential in the repassivation of aluminium alloys. Surf Interf Anal 2013; 45: 1575–1584.

Engelhardt G, Urquidi-Macdonald M, Macdonald DD. A simplified method for estimating corrosion cavity growth rates. Corros Sci 1996; 38: 1613–1635.

Frankel GS, Scully JR, Jahnes CV. Repassivation of pits in aluminum thin films. J Electrochem Soc 1996; 143: 1834–1840.

Guillaumin V, Mankowski G. Localized corrosion of 2024 T351 aluminium alloy in chloride media. Corros Sci 1998; 41: 421–438.

Gutman EM. Mechanochemistry of solid surfaces. New Jersey, Singapore, London: World Scientific Publishing Co. Pte. Ltd., 1994.

Holroyd NJH, Scamans GM. Crack propagation during sustained-load cracking of Al-Zn-Mg-Cu aluminum alloys exposed to moist air or distilled water. Metall Mater Trans A 2011; 42A: 2011–3979.

Hughes AE, Birbilis N, Mol JMC, Garcia SJ, Zhou X, Thompson GE. High strength Al-alloys: microstructure, corrosion and principles of protection. Ch. 10. In: Ahmad Z, editor. Recent trends in processing and degradation of aluminium alloys. Rijeka, Shangai: InTech Europe, 2011 (ISBN: 978-953-307-734-5).

Hughes AE, Parvizi R, Forsyth M. Microstructure and corrosion of AA2024. Corros Rev 2015; 33: 1–30.

Jilani O, Njah N, Ponthiaux P. Transition from intergranular to pitting corrosion in fine grained aluminum processed by equal channel angular pressing. Corros Sci 2014; 87: 259–264.

Jones DA. Localized surface plasticity during stress corrosion cracking. Corrosion 1996; 52: 356–362.

Knight SP, Birbilis N, Muddle BC, Trueman AR, Lynch SP. Correlations between intergranular stress corrosion cracking, grain-boundary microchemistry, and grain-boundary electrochemistry for Al–Zn–Mg–Cu alloy. Corros Sci 2010; 52: 4073–4080.

Knight SP, Pohl K, Holroyd NJH, Birbilis N, Rometsch PA, Muddle BC, Goswami R, Lynch SP. Some effects of alloy composition on stress corrosion cracking in Al–Zn–Mg–Cu alloys. Corros Sci 2015; 98: 50–62.

Lin YC, Liu G, Chen M, Zhang J, Chen Z, Jiang Y, Li J. Corrosion resistance of a two-stage stress-aged Al-Cu-Mg alloy: effects of external stress. J Alloys Comp 2016; 661: 221–230.

Little DA, Connolly BJ, Scully JR. An electrochemical framework to explain the intergranular stress corrosion behavior in two Al-Cu-Mg-Ag alloys as a function of aging. Corros Sci 2007; 49: 347–372.

Liu X, Frankel GS. Effects of compressive stress on localized corrosion in AA2024-T3. Corros Sci 2006; 48: 3309–3329.

Lynch S. Hydrogen embrittlement phenomena and mechanisms. Corros Rev 2012; 30: 105–123.

Meng Q, Frankel GS. Effect of Cu content on corrosion behavior of 7xxx series aluminum alloys. J Electrochem Soc 2004; 151: B271–B283.

Moore KL, Sykes JM, Grant PS. An electrochemical study of repassivation of aluminium alloys with SEM examination of the pit interiors using resin replicas. Corros Sci 2008; 50: 3233–3240.

Nguyen TH, Brown BF, Foley RT. On the nature of the occluded cell in the stress corrosion cracking of AA 7075-T651 – effect of potential, composition, morphology. Corrosion 1982; 38: 319–326.

Nisancioglu K, Holtan H. The protection potential of aluminum. Corros Sci 1978; 18: 1011–1023.

Nishijima Y, Oster G. Diffusion of glycerol-water mixture. Bull Chem Soc Japan 1960; 33: 1649–1651.

Okada T. Considerations of the stability of pit repassivation during pitting corrosion of passive metals. J Electrochem Soc 1984; 131: 1026–1032.

Pride ST, Scully JR, Hudson JL. Metastable pitting of aluminium and criteria for the transition to stable pit growth. J Electrochem Soc 1994; 141: 3028–3040.

Rehbinder PA, Shchukin ED. Surface phenomena in solids during deformation and fracture processes. Prog Surf Sci 1972; 3: 97–188.

Revie RW. Effects of dissolution on plastic deformation and cracking of metals. Prog Surf Sci 1983; 14: 53–112.

Sadananda K, Vasudevan AK. Review of environmentally assisted cracking. Metall Mater Trans A 2011; 42: 279–295.

Scully JC. The theory of stress corrosion cracking in alloys, 1st ed. UK: Maney and Son Ltd, 1971.

Sehgal A, Lu D, Frankel GS. Pitting in aluminum thin films supersaturation and effects of dichromate ions. Electrochem Soc 1998; 145: 2834–2840.

Sun R, Sun Q, Xie Y, Dong P, Chen Q, Chen K. Enhancing corrosion resistance of 7150 Al alloy using novel three-step aging process. Trans Nonferrous Met Soc China 2016; 26: 1201 – 1210.

Trueba M, Trasatti SP. Study of Al alloy corrosion in neutral NaCl by the pitting scan technique. Mater Chem Phys 2010; 121: 523–533.

Trueba M, Trasatti SP. Electrochemical approach to repassivation kinetics of Al alloys: gaining insight into environmentally assisted cracking. Corros Rev 2015; 33: 373–393.

Tyzak C. Fracture mechanics and stress corrosion cracking – a possible relationship between K_{Ic} and $K_{I(SCC)}$. Br Corros J 1971; 6: 219–223.

Wall FD, Stoner GE. The evaluation of the critical electrochemical potentials influencing environmentally assisted cracking of Al-Li-Cu alloys in selected environments. Corros Sci 1997; 39: 835–853.

Wang S, Frankel GS, Jiang J, Chen J, Dai S, Zhena L. Mechanism of localized breakdown of 7000 series aluminum alloys. J Electrochem Soc 2013; 160: C493–C502.

West JM. Chemical potential and surface energy in stress-corrosion cracking. Metal Sci 1980; 14: 534–540.

Yasuda M, Weinberg F, Tromans D. Pitting corrosion of Al and Al-Cu single crystals. J Electrochem Soc 1990; 137: 3708–3715.

Zhang W, Frankel GS. Transitions between pitting and intergranular corrosion in AA2024. Electrochim Acta 2003; 48: 1193–1210.

Ziman JM. Principles of the theory of solids. Cambridge: University Press, 1964.